

Double percolation effects and fractal behavior in magnetic/superconducting hybrids

L. Ruiz-Valdepeñas¹, M. Vélez², F. Valdés-Bango^{2,3}, L. M. Álvarez-Prado^{2,3}, J.I. Martín^{2,3}, E. Navarro¹, J. M. Alameda^{2,3} and J. L. Vicent^{1,4}

¹Dpto. Física de Materiales, Universidad Complutense, 28040 Madrid, Spain

²Depto. Física, Universidad de Oviedo, 33007 Oviedo, Spain

³CINN, (CSIC - Universidad de Oviedo - Principado de Asturias), Llanera, Spain

⁴IMDEA-Nanociencia, Cantoblanco, 28049 Madrid, Spain

E-mail: mvelez@uniovi.es

Abstract. Perpendicular magnetic anisotropy ferromagnetic/ superconducting (FM/SC) bilayers with a labyrinth domain structure are used to study nucleation of superconductivity on a fractal network, tunable through magnetic history. As clusters of reversed domains appear in the FM layer, the SC film shows a percolative behavior that depends on two independent processes: the arrangement of initial reversed domains and the fractal geometry of expanding clusters. For a full labyrinth structure, the behavior of the upper critical field is typical of confined superconductivity on a fractal network.

PACS numbers: 74.25.Dw; 75.70.-i

1. INTRODUCTION

Percolation phenomena are present in a wide variety of disordered systems, ranging from random networks [1] to nanomaterials [2], granular superconductors [3, 4] or perpendicular magnetic anisotropy materials [5]. Theoretical understanding of these phenomena has evolved from the classical analysis of simple regular lattices [6, 7] to more complex situations [8]. Recently, double percolation effects have been theoretically introduced [9] in order to describe systems such as polymer blends [10] or nanomaterials [2] in which disorder occurs on a two-level scale characterized by two different geometrical length scales.

Hybrid ferromagnetic/superconducting (FM/SC) multilayers and nanostructures are an interesting class of systems that are also governed by the competition between two different length scales [11]. The interplay between these two long range phenomena results in a rich variety of behaviors such as reentrant superconductivity [12], domain wall superconductivity (DWS) induced by the ferromagnetic exchange field [13, 14, 15], vortex guiding [16, 17, 18] or periodic vortex pinning [19]. Magnetic domains have been used to manipulate superconductivity both in parallel [14, 20] and perpendicular field configurations [21, 22]. In particular, stray fields created by a magnetic layer with perpendicular magnetic anisotropy (PMA) have proved a versatile tool to tune superconducting vortex pinning [23] and the superconducting phase diagram [24, 21], i.e. a controllable magnetic domain structure can be created playing with the magnetic layer hysteresis that, in turn, controls the nucleation of superconductivity. Up to now, most attention has centered on ordered domain geometries and on samples with relatively large magnetic domains in comparison with the Ginzburg-Landau coherence length ξ_{GL} [17, 25, 26, 27]. In these systems, due to field compensation effects, reentrant superconductivity is observed [12, 24, 25, 26, 27] and vortices can be nucleated on top of the magnetic domain structure [28, 29]. On the other hand, domains in PMA materials often display a very disordered labyrinthine structure [5, 30] and peaks in the magnetoresistance curves of PMA FM/SC multilayers have been reported as domain structure in the FM layer changed from an ordered to a disordered configuration indicating that the number and arrangement of domain walls can have a significant influence on superconductivity [22]. Actually, percolation phenomena have been found in FM/SC bilayers with a disordered domain structure in which, for large enough domains, the superconducting sample fraction was directly given by the reversed domains area [31]. However, taking into account that labyrinthine domain structures can be described in terms of a fractal geometry [32, 33], they could be used, for small enough domain sizes, to "design" a fractal network for the nucleation of superconductivity similarly to disordered superconducting wire networks (SWN) [34] and granular superconductors [3, 35]. Remarkably, this labyrinthine structure would allow to tune a fractal superconducting behavior through the magnetic film history.

In this work, we have studied PMA FM/SC bilayers with domain size below 100 nm, that becomes comparable to ξ_{GL} close to the critical temperature T_C . We

show that nucleation of superconductivity is controlled both by the distribution of clusters of reversed domains and their fractal geometry resulting in a double level percolation process. Once the percolation process is finished and the labyrinthine domain configuration extends homogenously through the sample, the upper critical field H_{c2} shows the characteristic temperature dependence of confined superconductivity on a fractal network.

2. EXPERIMENTAL

FM/SC NdCo/Nb bilayers have been fabricated by sputtering on $1\text{ cm} \times 1\text{ cm}$ Si(100) substrates in a two step process. First, a $\text{NdCo}_5(t\text{ nm})$ amorphous layer is grown by cosputtering [36, 37] with thickness (t) in the 40 - 80 nm range on a Si substrate covered by a 10 nm thick Al buffer layer and, then, a 5 nm thick Al capping layer is grown on top. Next, the Al/NdCo/Al sample is taken out of the chamber so that the Al capping layer becomes oxidized and, finally, a Nb film with thickness $d_{Nb} = 50\text{ nm}$ is grown on top by sputtering to get the complete FM/SC bilayer structure.

The properties of the SC layer have been characterized on a control 50 nm Nb film, grown on a bare Si substrate under similar conditions. It presents a $T_C = 7.55\text{ K}$, typical for Nb in this thickness range [38] and a Ginzburg-Landau coherence length $\xi_{GL}(0) = 8.95\text{ nm}$, obtained from the temperature dependence of $H_{c2} = \Phi_0/2\pi\xi_{GL}(T)^2$ with Φ_0 the quantum of flux. It corresponds to a superconducting coherence length $\xi_s = \frac{2}{\pi}\xi_{GL}(0) = 5.7\text{ nm}$ [39, 40].

The FM layer is made of NdCo_5 , an amorphous alloy with saturation magnetization $M_S \approx 10^3\text{ emu/cm}^3$. It presents a moderate room temperature (RT) perpendicular magnetic anisotropy, that can be characterized by an out-of-plane uniaxial anisotropy constant [41] (K_n), with values of the order $K_n \approx 10^6\text{ erg/cm}^3$. Upon lowering the temperature, K_n increases up to $K_n \approx 10^7\text{ erg/cm}^3$ at 10 K [37], that is, the anisotropy ratio $Q = K_n/2\pi M_S^2$ is $Q \approx 0.1$ at room temperature and $Q \approx 1$ at 10 K.

In general, proximity effects between the FM and SC layers could be caused both by exchange and stray fields. In the present case, for $Q \approx 1$, the domain structure in the PMA Nd-Co layer should contain significant out-of-plane magnetization components that can be used to create relatively large stray fields in the neighbouring Nb layer. On the other hand, the oxidized AlO_x layer in between Nb and NdCo layers should act as an exchange-field insulator so that proximity effects due to the exchange field in the FM layer should be small. Also, $d_{Nb} \gg \xi_s$ in these films implying that exchange induced DWS should be strongly suppressed [15]. In any case, the aim of our study is mainly on the effect of geometry on the superconducting regions that nucleate on top of the magnetic domains rather than on the specific proximity effect mechanism (exchange field and/or stray field) involved to create them.

Magnetic and superconducting properties of the SC/FM bilayers have been studied by magnetotransport measurements in a He cryostat equipped with a 90 kOe superconducting solenoid and a rotatable sample holder that allows to vary *in-situ*

the applied field direction from in-plane to out-of-plane. Transport measurements are performed on extended samples using a four probe DC technique in a van der Pauw configuration[42, 43] which is often used in percolation problems [44, 45, 46] with an applied current ($I_{DC} = 10-100\mu A$). Depending on whether voltage and current contacts are consecutive or crossed along the sample edge either the resistance R or Hall effect R_{Hall} signals can be obtained from exactly the same sample area [42].

First, the magnetic properties of the FM layer have been obtained from Hall effect measurements making use of the much larger Hall effect in ferromagnetic materials [47] than in ordinary metals such as Nb. Briefly, in a FM layer with an out-of-plane magnetization component M_z under a perpendicular field H_z , the Hall signal (R_{Hall}) is given by $R_{Hall} = R_0 H_z + R_{EHE} M_z$, with R_0 the ordinary Hall effect coefficient, related with the deviation of charge carriers by the Lorentz force, and R_{EHE} the Extraordinary Hall effect (EHE) coefficient, related with spin dependent scattering of conduction electrons [47]. R_{EHE} is usually much larger than R_0 (about a factor 10-100) and is particularly enhanced in Rare Earth-Transition Metal amorphous alloys due to their large resistivities and strong spin-orbit coupling [48]. Thus, Hall effect hysteresis loops of the FM/SC bilayers should be dominated by the EHE term $R_{EHE} M_z$ in the Nd-Co layer [48, 49]. This procedure allows us to characterize the FM layer magnetic properties at 10 K, just above T_c , and, also, to control its magnetic history *in situ* by performing different kinds of minor hysteresis loops. Then, once the sample has been prepared in the desired magnetic state at 10K, its superconducting properties have been characterized measuring resistance transitions ($R(T)$ curves) as the temperature is lowered under a constant out-of-plane magnetic field H_z .

3. RESULTS AND DISCUSSION

3.1. Magnetic properties and stray field of the NdCo FM layers

Hysteresis loops in PMA films can have a variety of shapes depending on the relative strength of PMA, exchange and disorder [50]. Figure 1 shows the EHE out-of-plane loop for a 52 nm NdCo/Nb sample measured at 10 K, i.e. just above T_C . It presents the characteristic shape of magnetization reversal through the nucleation and expansion of clusters of stripe domains [50, 51]: upon decreasing H_z from saturation, R_{Hall} follows a weak linear field dependence due to ordinary Hall effect while small reversed domains begin to nucleate across the sample; then, there is a steep decrease in R_{Hall} already at positive fields, between $3.4 \text{ kOe} > H_z > 2.1 \text{ kOe}$, that marks the sudden growth of clusters of labyrinth stripe domains until they fill the whole sample area; next, there is an almost reversible regime in which R_{Hall} decreases linearly with H due to relative changes in the width of "up" and "down" domains and the film displays a very low remanence and coercivity. Finally, as domains with the initial magnetization are annihilated, negative saturation is reached. Upon increasing the temperature up to RT, the decrease in PMA in the Nd-Co films results in an enhancement of the low field reversible region while

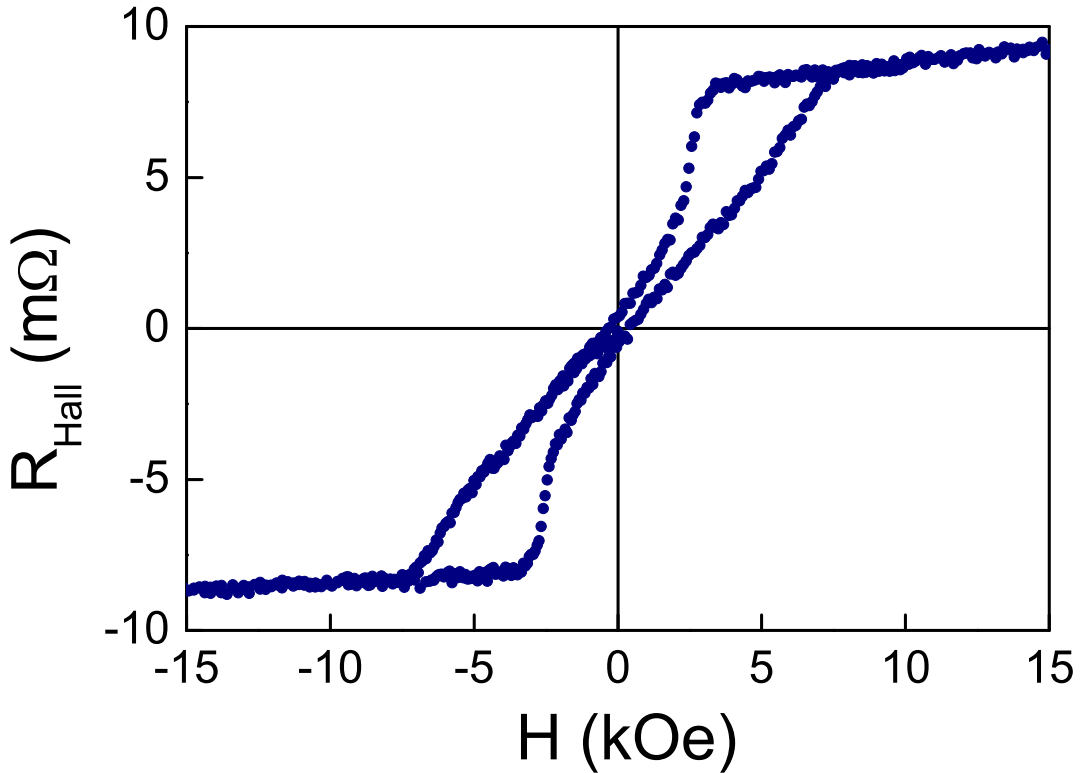


Figure 1. (color online) EHE hysteresis loop of a 52 nm NdCo/50 nm Nb bilayer at 10K. Note that a constant resistance offset $R_{offset} = 1.2\Omega$ due to contact misalignment has been subtracted to obtain R_{Hall} from raw resistance measurements.

high field hysteresis almost disappears [52]. Both the remanent magnetization (M_R) and coercivity (H_{coer}) stay almost constant at very low values in the whole temperature range from 10K to RT (M_R below $0.05M_S$ and H_{coer} below 0.5 kOe) indicating that there should not be qualitative changes between the room temperature and the 10 K remanent domain structure.

Figures 2(a) and (b) show the differences in the remanent domain configurations of NdCo films depending on their previous magnetic history, obtained by Magnetic Force Microscopy (MFM) at room temperature [36]: in the first case (figure 2(a)), an in-plane field $H_y = 1$ kOe has been applied to a 45 nm thick NdCo sample and, then, it has been decreased to zero creating the typical parallel stripe domain structure oriented along H_y with stripe domain period $\Lambda = 115$ nm; in the second case (figure 2(b)), a labyrinthine domain configuration is observed in an 80 nm thick NdCo film after saturation with an out-of-plane $H_z = 4$ kOe. Λ values obtained from the RT MFM characterization depend on t and H , but they are in the 100 nm - 300 nm range for the studied samples [36, 49].

The effect of the temperature dependence of K_n on the low temperature domain structure has been studied by micromagnetic simulations [53]. First, material parameters have been adjusted to reproduce the observed RT domain structure and,

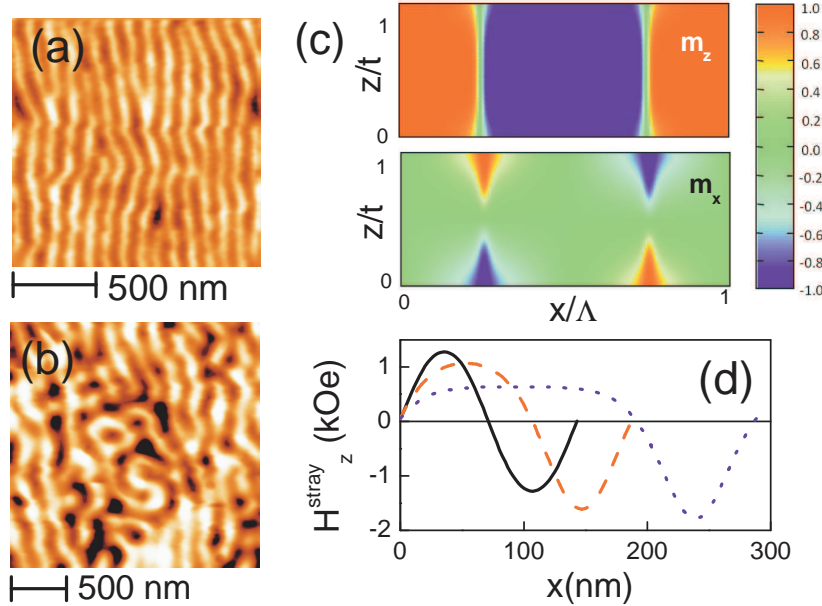


Figure 2. (color online) (a) MFM image of a 45 nm NdCo film at remanence after applying an in-plane $H_y = 1$ kOe ($\Lambda = 115$ nm); (b) MFM image of a 80 nm NdCo film at remanence after applying an out-of-plane $H_z = 4$ kOe; (c) Map of the simulated magnetization distribution of a 52 nm NdCo film at remanence: top panel, out-of-plane m_z and bottom panel, in-plane m_x . Note the reduced scale for spatial variables, z/t and x/Λ ($t = 52$ nm and $\Lambda = 143$ nm). Color code of m_x and m_z values is indicated in left scale bar. (d) Simulated $H_z^{\text{stray}}(x)$ created by a 52 nm NdCo film at $h = 30$ nm plotted over one stripe period Λ for: $H_z = 0$, solid line; $H_z = 3$ kOe, dashed line; $H_z = 4.5$ kOe, dotted line.

then, the temperature variations of K_n and M_S have been introduced in order to calculate the low temperature equilibrium parallel stripes domain configuration, that is quite similar to RT but with a small increment in Λ (about 10%). Figure 2(c) shows a map of the magnetization distribution (out-of-plane $m_z = M_z/M_s$ and in-plane

$m_x = M_x/M_s$) obtained for a 52 nm NdCo film at 10 K calculated with anisotropy constant $K_n = 5.6 \times 10^6$ erg/cm³, magnetization $M_s = 897$ emu/cm³, and exchange $A = 10^6$ erg/cm at $H_z = 0$. Top panel in figure 2(c) shows the typical alternating "up"/"down" domains in m_z separated by Bloch walls that make up the periodic parallel stripe configuration with $\Lambda = 143$ nm. Domain wall width δ_w at the film surface can be estimated from the size of the region in which m_z turns from 1 to -1. It is about 40 nm in the simulations with RT parameters and goes down to 18 nm at low temperature. Bottom panel in figure 2(c) allows us to observe the existence of Neel caps on top of the Bloch walls in which M becomes parallel to the film surface. Thus, due to the moderate PMA of these films, the domain structure is quite different from previously studied PMA FM/SC systems ($Q \gg 1$) [27]. It not only contains parallel regions with oscillating out-of-plane magnetization component but, as well, a relatively large flux-closure structure of Neel caps close to the film surface that significantly weakens the stray field.

Now, we can calculate the stray field H_z^{stray} created by the simulated parallel stripe domain structure in the space above the FM layer. figure 2(d) is a plot of the stray field profile at the mid-plane of the Nb film (at a height $h = 30$ nm) starting from the equilibrium remanent state ($H = 0$) and, then, upon applying an out-of-plane field H_z of increasing magnitude. At remanence, H_z^{stray} displays a symmetric profile with period $\Lambda = 143$ nm. Then, as H_z increases, the stray field profile becomes asymmetric due to the growth of positive domains at the expense of the negative ones and Λ becomes larger going up to 288 nm at 4.5 kOe. At the same time, as the size of negative domains shrinks, the average negative $\langle H_z^{stray} \rangle$, calculated as the spatial average of H_z^{stray} over the negative domain region, is enhanced from -825 Oe at remanence to -1 kOe at $H_z = 4.5$ kOe.

3.2. Superconducting transitions and percolation effects

Figure 3 shows the superconducting transitions measured on the 52 nm NdCo/Nb bilayer at a constant H_z , following different hysteresis paths in the magnetic layer as indicated in figure 3(a). One of them is a major hysteresis loop (ML, \circ): a large $H_z = 20$ kOe is applied to the sample in order to reach an out-of-plane saturated state and, then, R(T) curves are measured at decreasing H_z values. The other two processes are minor hysteresis loops. In the first minor loop (mL₁, \blacktriangledown), H_z starts at -20 kOe, i.e. with the sample at the negative out-of-plane saturated state, then it increases up to $H_1 = 7.2$ kOe which is the field at which irreversibility disappears in the loop but is not large enough to ensure full out-of-plane saturation (i.e. small inverted domains could still persist in the sample with a very small contribution to the magnetization [51]) and, finally, R(T) curves are measured as H_z decreases from H_1 . In the second minor loop (mL₂, \blacksquare) H_z starts at 20 kOe, i.e. with the sample at the positive out-of-plane saturated state, then H_z is taken down to $H_2 = 2.6$ kOe in order to bring the sample to the initial stages of reversed domain expansion and, then, R(T) curves are measured as H_z

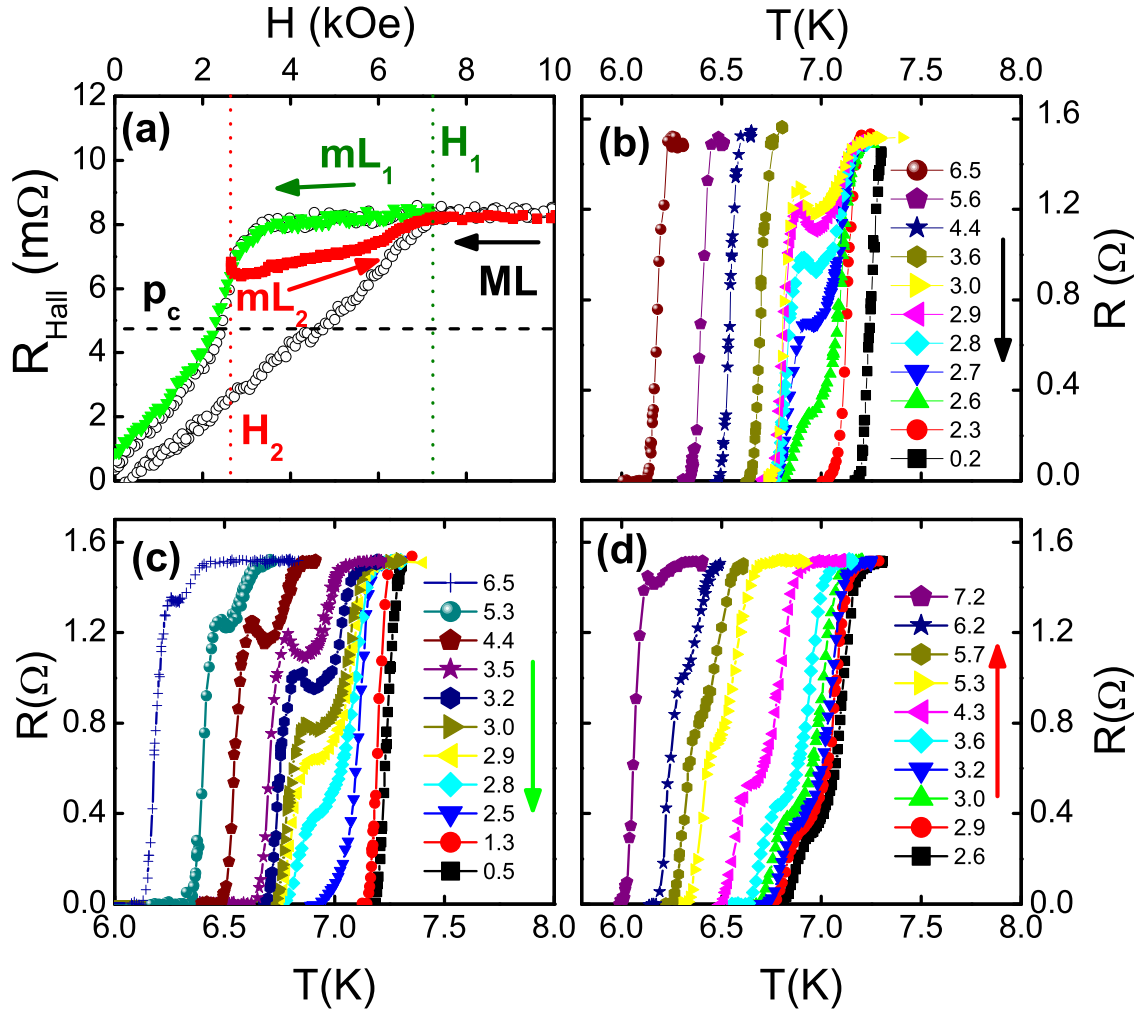


Figure 3. (color online)(a) EHE loops of a 52 nm NdCo/50 nm Nb bilayer at 10K along three hysteresis processes: \circ , Major loop (ML), measured as H_z decreases from saturation at 20 kOe; \blacktriangledown , minor loop 1 (mL_1), measured as H_z decreases from incomplete saturation at $H_1 = 7.2$ kOe; \blacksquare , minor loop 2 (mL_2), H_z goes down from 20 kOe to $H_2 = 2.6$ kOe and, then, R_{Hall} is measured upon increasing H_z . Dashed line indicates the signal level at 2.45 kOe (i.e. at the percolation threshold in ML), used to estimate p_c as indicated in the text. Sets of consecutive $R(T)$ curves at constant H_z , measured along (b) ML; (c) mL_1 and (d) mL_2 . Labels indicate H_z in kOe at each $R(T)$.

increases so that the reversed area fraction must shrink again. In all the cases there is a certain field range in which the superconducting transitions develop a two-step structure, characteristic of the break up of the sample in two kinds of regions with different T_C 's (T_{C1} and T_{C2}). At intermediate temperatures, $T_{C1} < T < T_{C2}$, conduction takes place by percolation through the network of coexisting superconducting and normal regions

within the sample [31, 54]. It is interesting to note that the field range of occurrence of this two-step percolative behavior is completely different between the major loop (3 kOe $\geq H_z \geq 2.5$ kOe) and mL₁ (6.5 kOe $\geq H_z \geq 2.8$ kOe) in spite of the almost identical $R_{Hall}(H_z)$ curves. This can be directly attributed to the small reversed domains present in the FM layer due to incomplete saturation during mL₁ loop that serve as nucleation centers for superconductivity in a wider field range.

A more detailed analysis of the two step transitions is shown in figure 4 in which the temperature dependence of the upper critical field $H_{c2}(T)$ is plotted. The phase boundary for superconductivity is usually obtained from $R(T)$ curves [12, 24, 18, 55, 56] as the points in the $H - T$ plane in which R is a certain fraction of the normal state resistance R_n . In this case, we have used two different resistance criteria $0.1R_n$ (to obtain $H_{c2}^{0.1R_n}(T)$) and $0.9R_n$ (to get $H_{c2}^{0.9R_n}(T)$), in order to characterize the two different kinds of regions present in the sample. For the major loop ML (figure 4(a)), both curves run essentially parallel at high and low fields at 0.1 K distance. This is similar to the transition width of plain reference Nb films indicating that there is essentially no field broadening of the superconducting transitions whenever the FM/SC bilayer is in a homogeneous state. However, at intermediate fields they become clearly separated as steps develop in the $R(T)$ curves: below 3 kOe, there is a sudden jump in $H_{c2}^{0.9R_n}(T)$ from the typical linear dependence ($H_{c2} = 41.2$ kOe $(1 - T/T_C)$) to a different non-linear temperature dependence that could be an indication of confined superconductivity [7, 3]; $H_{c2}^{0.1R_n}(T)$ follows a similar trend but it retains the linear temperature dependence down to 2.5 kOe. That is, percolation effects appear approximately in the field range corresponding to the nucleation/expansion of clusters of reversed domains (shaded areas in figure 4). The different temperature dependence of $H_{c2}^{0.9R_n}$ and $H_{c2}^{0.1R_n}$ for 3 kOe $> H > 2.45$ kOe is a signature of qualitative differences between the coexisting normal/superconducting regions during the percolation process: $H_{c2}^{0.9R_n}$ corresponds to confined superconducting regions that nucleate on top of clusters of reversed domains (see sketch in figure 4(a)) whereas $H_{c2}^{0.1R_n}$ marks the transition of the surrounding extended areas that retain the same dimensionality as the continuous film. Then, for $H < 2.45$ kOe, steps in $R(T)$'s disappear as the confined superconducting areas percolate through the sample effectively shorting the possible remaining extended normal regions. The reversed area fraction p_{mag} at each point of the hysteresis loop can be estimated as $p_{mag} = 0.5(1 - M/M_S)$. Thus, the percolation threshold p_c would correspond to p_{mag} at 2.45 kOe, i.e. $p_c \approx 0.2$.

The qualitative differences between $H_{c2}^{0.9R_n}(T)$ and $H_{c2}^{0.1R_n}(T)$ are more evident in figures 4 (b) and (c) corresponding to minor loops mL₁ and mL₂. Now, due to FM film history, reversed domains and, therefore, steps in $R(T)$ curves are present in a wider field range, which allows for a more thorough analysis of the percolation process. According to classical percolation theory in 2D [57], the resistance of a random mixture of superconducting/normal elements scales with the superconducting fraction p_{sup} as

$$R \propto (p_c - p_{sup})^s \quad (1)$$

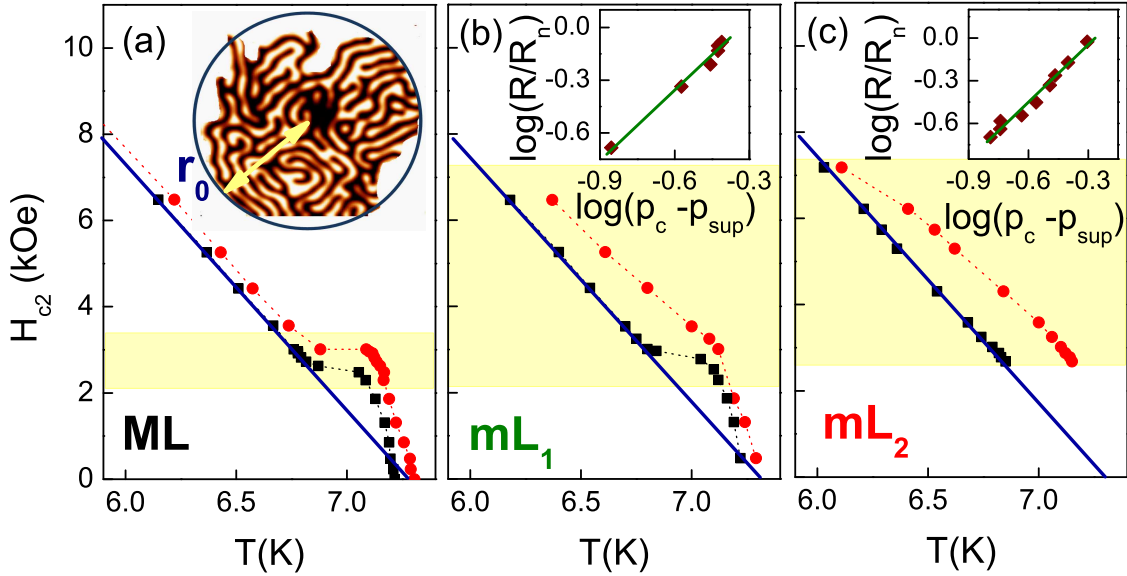


Figure 4. (color online) H_{c2} vs. T defined at $0.1R_n$ (■) and at $0.9R_n$ (●) measured along (a) ML (b) mL₁ and (c) mL₂. Solid lines are linear fits to $H_{c2} = 41.2$ kOe($1 - T/T_C$). Shaded areas mark field range of nucleation/expansion of inverted domains obtained from EHE loops. Inset in (a) is a sketch of a cluster of inverted domains. Insets in (b) and (c) are log-log plots of R/R_n at the plateaus in $R(T)$ vs. $(p_c - p_{sup})$.

with universal exponent $s = 1.3$. The percolation threshold is $p_c = 0.5$ for square lattice models, but it can vary significantly depending on system geometry [58]. However, the resistance values at the "plateaus" in $R(T)$ curves in figure 3 cannot be described by eq. (1) using the simplest assumption $p_{sup} = p_{mag}$ that was used in Nb/BaFeO hybrids with much larger domain sizes [31]. This is reasonable since, the comparison between ML and mL₁ data directly shows that effective superconducting area is not simply proportional to the inverted domain area but depends on the previous magnetic history (i.e. on the initial distribution of reversed domains). Also, the small observed $p_c \approx 0.2$ is typical of two-level percolation [9, 10] in which two independent random processes are at play (reversed domain nucleation and propagation in the PMA film here [30]). In the first level, we may consider a random arrangement of initial reversed nuclei and, on the second level with a finer length scale, the fractal expansion of each cluster of reversed domains starting from each initial nucleus [30, 32, 33]. Thus, along the superconducting transition, the Nb film will be composed of a random array of SC islands nucleated on each of these clusters of reversed domains. For a labyrinth domain structure, we may consider that the effectively shorted area for each SC island is that of a disk enclosing the cluster [59] (see sketch in figure 4(a)). The radius of this circle r_0 scales as $p_{mag} \propto r_0^{D_m}$ with D_m the mass dimension of the cluster [30] ($D_m = 1.896$ for an infinite cluster [58] and $D_m \approx 1.5 - 2$ reported for expanding clusters of reversed domains in amorphous

Rare Earth-Transition Metal alloys [30]). Thus, the area of SC islands should scale as $p_{sup} \propto r_0^2 \propto (p_{mag})^{2/D_m}$. Insets in figures 4 (b) and (c) show the results of the fit of R vs. $p_{sup} = (p_{mag})^{2/D_m}$ to equation (1). A linear behavior in the log-log plot appears for $D_m = 1.8$, close to the mass dimension of an infinite cluster, and $s = 1.32 \pm 0.07$, in good agreement with the critical exponent expected from 2D percolation theory [57]. s and D_m are similar both for mL_1 and mL_2 but certain differences appear in the fitted thresholds $p_c(mL_1) = 0.16$ and $p_c(mL_2) = 0.21$, which may be attributed to the different distribution of initial reversed nuclei in each hysteresis process.

3.3. Upper critical field dimensionality

Further confirmation on the fractal geometry of the superconductivity phase nucleated on top of the labyrinth reversed domains may be obtained from the analysis of the temperature dependence of H_{c2} , focusing in the homogeneous regime after the percolation process is finished and steps have disappeared from the $R(T)$ transitions. Figure 5 shows several $H_{c2}^{0,1R_n}(T)$ lines measured along different hysteresis processes. First, there are two out-of-plane major loops both in the descending and ascending field branches: $ML1(-)$ with H_z decreasing from saturation at 20 kOe, $ML1(+)$ with H_z increasing from remanence after saturation at -20 kOe, $ML2(-)$ with H_z decreasing from saturation at 90 kOe, $ML2(+)$ with H_z increasing from remanence after saturation at -90 kOe. Data are also included upon increasing H_z from different remanent states: $Demag1(+)$ and $Demag2(+)$ correspond to out-of-plane demagnetized states after performing a series of H_z cycles of decreasing amplitude in order to create a disordered labyrinth domain pattern over the whole sample and $Ordered(+)$ corresponds to an in-plane remanent state after applying an in-plane $H_y = 90$ kOe in order to create an ordered parallel stripes configuration perpendicular to the applied current direction. In the two descending field processes $ML1(-)$ and $ML2(-)$, steps in the $R(T)$ transition disappear below 2.5 kOe, as discussed above, indicating that the lower field region corresponds to a fully percolated labyrinthine state. On the other hand, in all the other ascending field processes no steps have been observed in the $R(T)$ transitions indicating that their initial remanent state covers the sample homogeneously. Thus, the data in figure 5 will allow us to study the characteristic dimensionality of the superconducting state nucleated on top of different homogeneous domain structures. It can be seen that these $H_{c2}^{0,1R_n}(T)$ curves are strongly dependent on magnetic history but present a common crossover at $H_z^* = 0.8$ kOe: the processes with stronger H_{c2} enhancement at high fields present also the lower $T_C(H = 0)$. However, in the reduced temperature scale $1 - T/T_C$, $H_{c2}^{0,1R_n}$ data become grouped in three distinct sets (see figure 5 (b)) depending on stripe domain geometry: one of them ($Ordered(+)$) corresponds to H_z increasing from remanence after in-plane saturation, i.e. from an ordered parallel stripe remanent state, and the other two correspond to labyrinth domain configurations either as H_z decreases below the percolation threshold ($ML1(-)$ and $ML2(-)$) or as H_z increases from remanence after out-of-plane negative saturation or demagnetization ($ML1(+)$,

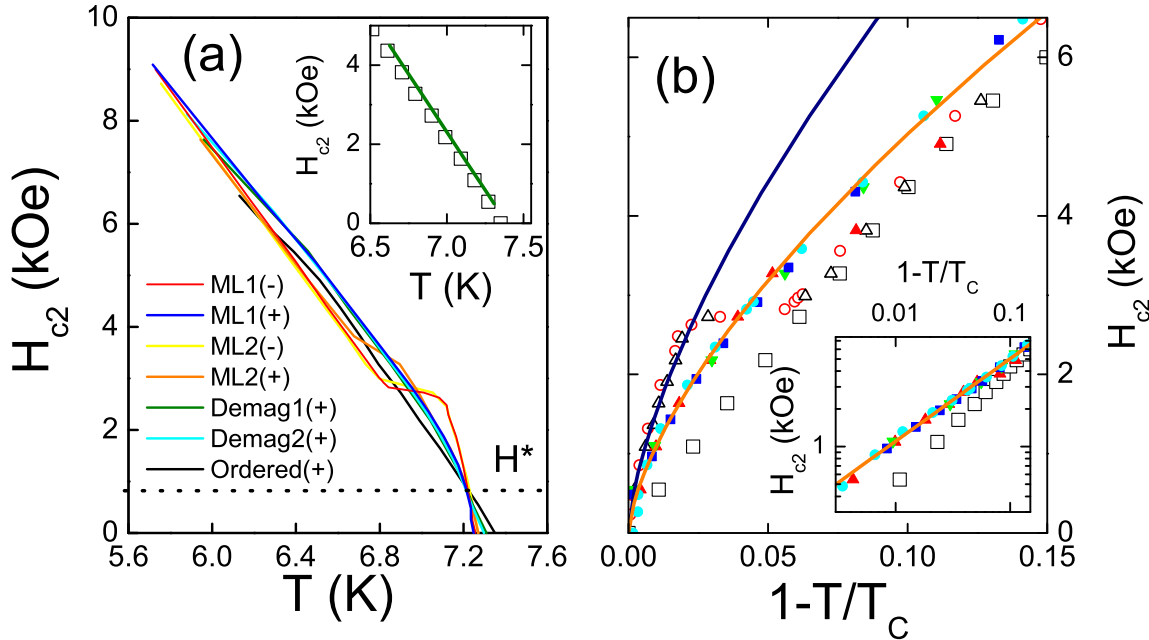


Figure 5. (color online) (a) $H_{c2}^{0.1R_n}(T)$ measured following different hysteresis process in the magnetic layers. Note the crossover at $H^* = 0.8kOe$. Inset shows $H_{c2}^{0.1R_n}(T)$ upon increasing H_z after in-plane saturation(\square , Ordered(+)) in comparison with the simulated dependence with a 1D model for a FM/SC bilayer with $\langle H_z^{stray}(h = 55 \text{ nm}) \rangle$ (solid line); (b) $H_{c2}^{0.1R_n}$ vs. $1 - T/T_c$. Parallel stripes remanent state: \square , Ordered(+); labyrinthine states: \circ , ML1(-); \triangle , ML2(-); \blacktriangledown , Demag1(+); \blacksquare , Demag2(+); \bullet , ML1(+); \blacksquare , ML2(+). Solid lines are fits to $H_{c2} \propto (1 - T/T_c)^n$ with $n = 0.66$. Inset shows same temperature dependence in a log-log scale.

ML2(+), Demag1(+) and Demag2(+)).

$H_{c2}(T)$ in the parallel stripes case can be analyzed in terms of existing stray field induced superconductivity models for SC/FM bilayers with an ordered lateral geometry [26, 27]. In particular, we have used a 1D model in the small domain size limit [27] complemented with the stray field values obtained from the micromagnetic calculations. Nucleation of superconductivity is determined by field confinement effects within a length scale L_H so that the upper critical field is given by the condition $\xi_{GL}(T) \approx L_H$. Taking into account the superposition of the stray field created by the FM layer H_z^{stray} with the applied field H_z , L_H is given by [27]

$$L_H = (\Phi_0/2\pi|H_z - H_z^{stray}|)^{1/2}. \quad (2)$$

In our case, H_z^{stray} is a function of H_z , as shown in figure 2(d), so that equation (2) allows to estimate H_{c2} through the implicit condition $H_{c2}(T) = H_z^{stray}(H_{c2}) + \Phi_0/2\pi\xi_{GL}(T)^2$. Best fit is obtained taking $H_z^{stray}(H_z)$ from the micromagnetic calculations at the top surface of the Nb film, $H_z^{stray} = \langle H_z^{stray}(h = 55 \text{ nm}) \rangle$ (see solid line in the inset of figure 5(a)). This is reasonable since nucleation of superconductivity should be favored at the top SC film surface in which the superconducting order parameter is maximum [27]. At low fields, L_H increases and, eventually, becomes larger than domain size,

so that the superconducting wave function extends over several domains and any H_{c2} enhancement due to the stray field disappears since it is averaged over positive and negative domains [27]. There is still a certain $T_C(H = 0)$ reduction due to the inhomogeneity introduced in the system by the periodic domain structure [26]. At the crossover field found in figure 5(a), $H_z^* = 0.8$ kOe, $\xi_{GL} = 63$ nm and $L_H^* = 75$ nm, which are comparable to domain size $\Lambda/2 = 71.5$ nm, indicating that it can correspond to the crossover from extended to localized superconductivity: more disordered domain structures with a stronger stray field present a larger H_{c2} enhancement in the high field range of localized superconductivity over reversed domains but, also, a more important $T_C(H = 0)$ reduction in the low field extended superconductivity regime.

Finally, let us focus on the two sets of $H_{c2}^{0,1R_n}$ data in figure 5(b) measured with labyrinth domain configurations that present a different behavior from the simple 1D ordered parallel stripe geometry. In spite of the differences in magnetic history (either out-of-plane saturated or out-of-plane demagnetized initial state), all these data follow clearly a stronger temperature dependence $H_{c2} \propto (1 - T/T_C)^n$ than expected for a 2D superconducting film in a perpendicular field geometry. In both cases the same H_{c2} exponent $n = 0.66$ is found, indicating that it is an intrinsic property of the labyrinth domain geometry. It lies in between 2D and 1D values $n = 1$ and 0.5 , respectively, and is similar to reported values in granular superconductors [3, 35] and disordered SWN [34]. This reduced H_{c2} exponent has been attributed to the fractal nature of the percolation networks [7], with $n = 0.69$ predicted for the infinite cluster, in good agreement with the experimental results in figure 5.

4. CONCLUSIONS

In summary, the disordered labyrinth domain structure of PMA NdCo layers have been used to "imprint" a fractal geometry in the superconducting state of NdCo/Nb bilayers. Superconducting transitions display a characteristic percolative behavior with the Nb film broken up into a mixture of extended normal regions and islands of confined superconductivity. The distribution and size of these islands is controlled by a two level percolation process: first, by the random distribution of initial reversed nuclei determined by magnetic film history and, second, by the fractal expansion of each cluster of reversed domains resulting in a larger effective superconducting area. The dimensionality of $H_{c2}(T)$ lines can also be tuned by magnetic film history: when it adopts a parallel stripe domain configuration, $H_{c2}(T)$ can be described by a simple model of field confinement with a 1D domain pattern; however, when domains adopt a labyrinth geometry, H_{c2} displays a stronger temperature dependence $H_{c2} \propto (1 - T/T_C)^{0.66}$ characteristic of fractal superconducting networks.

Acknowledgments

Work supported by Spanish MINECO under grants FIS2008-06249, Consolider CDS2007-00010 and CAM grant S2009/MAT-1726. LRV acknowledges support from a FPU fellowship.

References

- [1] Q. Cao, H. Kim, N. Pimparkar, J. P. Kulkarni, C. Wang, M. Shim, K. Roy, M. A. Alam and J. A. Rogers, *Nature* **454**, 495 (2008).
- [2] K. Na, C. Jo, J. Kim, K. Cho, J. Jung, Y. Seo, R. J. Messinger, B. F. Chmelka and R. Ryoo, *Science* **333**, 328 (2011).
- [3] A. Gerber and G. Deutscher, *Phys. Rev. Lett.* **63**, 1184 (1989).
- [4] X. Liu, R. P. Panguluri, Z.F. Huang and B. Nadgorny, *Phys. Rev. Lett.* **104**, 035701 (2010).
- [5] J. P. Attané, Y. Samson, A. Marty, J. C. Toussaint, G. Dubois, A. Mougin and J. P. Jamet, *Phys. Rev. Lett.* **93**, 257203 (2004).
- [6] D. Stauffer and A. Aharony, *Introduction to Percolation Theory* (Taylor and Francis, London 2003).
- [7] S. Alexander, *Phys. Rev. B* **27**, 1541 (1983).
- [8] A. Haji-Akbari and R. M. Ziff, *Phys. Rev. E* **79** 021118 (2009).
- [9] J. Li, B. Ray, M. A. Alam and M. Östling, *Phys. Rev. E* **85**, 021109 (2012).
- [10] K. Levon, A. Margolina and A. Z. Patashinsky, *Macromolecules* **26**, 4061 (1993).
- [11] For a review see A. I Buzdin, *Rev. Mod. Phys.* **77**, 935 (2005) and references therein.
- [12] Z. Yang, M. Lange, A. Volodin, R. Szymczak and V. V. Moshchalkov, *Nat. Mater.* **3**, 793 (2004).
- [13] A. I. Buzdin, L. N. Bulaevskii and S. V. Panyukov, *Sov. Phys. JETP* **60**, 174 (1984).
- [14] A. Yu. Rusanov, M. Hesselberth, J. Aarts and A. I. Buzdin, *Phys. Rev. Lett.* **93**, 057002 (2004)
- [15] M. Houzet and A. I. Buzdin, *Phys. Rev. B* **74**, 214507 (2006).
- [16] M. Velez, D. Jaque, J. I. Martin, M. I. Montero, Ivan K. Schuller and J. L. Vicent, *Phys. Rev.B* **65**, 104511 (2002).
- [17] V. Vlasko-Vlasov, U. Welp, G. Karapetrov, V. Novosad, D. Rosenmann, M. Iavarone, A. Belkin and W.-K. Kwok, *Phys. Rev. B* **77**, 134518 (2008)
- [18] A. Belkin, V. Novosad, M. Iavarone, J. Fedor, J. E. Pearson, A. Petrean-Troncalli and G. Karapetrov, *Appl. Phys. Lett.* **93**, 0725510 (2008).
- [19] M. Velez, J. I. Martin, J. E. Villegas, A. Hoffmann, E.M. Gonzalez, J.L. Vicent and Ivan K. Schuller, *J. Magn. Magn. Mater.* **320**, 2547 (2008).
- [20] D. Stamopoulos and M. Pissas, *Phys. Rev. B* **73**, 132502 (2006).
- [21] W. Gillijns, A. Yu. Aladyshkin, A. V. Silhanek and V. V. Moshchalkov, *Phys. Rev. B* **76**, 060503 (2007).
- [22] L. Y. Zhu, T. Y. Chen and C. L. Chien, *Phys. Rev. Lett.* **101**, 017004 (2008).
- [23] A. Gomez, D. A. Gilbert, E. M. Gonzalez, Kai Liu and J. L. Vicent *Appl. Phys. Lett.* **102**, 052601 (2013).
- [24] L. Y. Zhu, M. Z. Cieplak and C. L. Chien, *Phys. Rev. B* **82**, 060503 (2010).
- [25] Z. Yang, J. Fritzsche and V. V. Moshchalkov, *Appl. Phys. Lett.* **98**, 012505 (2011).
- [26] A. Yu. Aladyshkin, A. I. Buzdin, A. A. Fraerman, A. S. Mel'nikov, D. A. Ryzhov and A. V. Sokolov, *Phys. Rev. B* **68**, 184508 (2003).
- [27] A. Yu. Aladyshkin and V. V. Moshchalkov, *Phys. Rev. B* **74**, 064503 (2006).
- [28] M. Iavarone, A. Scarfato, F. Bobba, M. Longobardi, G. Karapetrov, V. Novosad, V. Yefremenko, F. Giubileo and A. M. Cuocolo, *Phys. Rev. B* **84**, 024506 (2011).
- [29] M. Z. Cieplak, Z. Adamus, M. Konczykowski, L. Y. Zhu, X. M. Cheng and C. L. Chien, *Phys. Rev. B* **87**, 014519 (2013).
- [30] A. Lyberatos, J. Earl and R. W. Chantrell, *Phys. Rev. B* **53**, 5493 (1996)

- [31] Z. Yang, K. Vervaeke, V. V. Moshchalkov and R. Szymczak, Phys. Rev. B **73**, 224509 (2006).
- [32] B. S. Han, D. Li, D. J. Zheng and Y. Zhou, Phys. Rev. B **66**, 014433 (2002).
- [33] C. Bathany, M. Le Romancer, J. N. Armstrong and H. D. Chopra, Phys. Rev. B **82**, 184411 (2010).
- [34] J. M. Gordon, A. M. Goldman and B. Whitehead, Phys. Rev. Lett. **59**, 2311 (1987); A.-L. Eichenberger, J. Affolter, M. Willemann, M. Mombelli, H. Beck, P. Martinoli and S. E. Korshunov, Phys. Rev. Lett. **77**, 3905 (1996).
- [35] K. Yamada, H. Fujiki, B. Shinozaki and T. Kawaguti, Physica C **355**, 147 (2001).
- [36] A. Hierro-Rodriguez, R. Cid, M. Velez, G. Rodriguez-Rodriguez, J. I. Martín, L. M. Alvarez-Prado and J. M. Alameda, Phys. Rev. Lett. **109**, 117202 (2012)
- [37] R. Cid, G. Rodriguez-Rodriguez, L. M. Alvarez-Prado, J. Diaz and J. M. Alameda, J. Magn. Magn. Mat. **316**, e446 (2007)
- [38] M. S. M. Minhaj, S. Meepagala, J. T. Chen, and L. E. Wenger, Phys. Rev. B **49**, 15235 (1994).
- [39] Z. Radović, L. Dobrosavljević-Grujić, A. I. Buzdin and J. R. Clem, Phys. Rev. B **38**, 2388 (1988).
- [40] A. Alija, D. Pérez de Lara, E. M. Gonzalez, G. N. Kakazei, J. B. Sousa, J. P. Araujo, A. Hierro-Rodriguez, J. I. Martín, J. M. Alameda, M. Vélez, and J. L. Vicent Phys. Rev. B **82**, 184529 (2010).
- [41] A. Hubert and R. Schäfer, *Magnetic Domains*, (Springer-Verlag, Berlin, 1998).
- [42] L. J. van der Pauw, Philips Res. Rep. **13**, 1 (1958).
- [43] M. Cagigal, J. Fontcuberta, M. A. Crusellas, J. L. Vicent, and S. Piñol Phys. Rev. B **50**, 15993 (1994).
- [44] R. Schad, S. Heun, T. Heidenblut, and M. Henzler, Phys. Rev. B **45**, 11430 (1992).
- [45] S. Das Sarma, M. P. Lilly, E. H. Hwang, L. N. Pfeiffer, K.W. West, and J. L. Reno, Phys. Rev. Lett. **94**, 136401 (2005).
- [46] H. M. Aarbogh, J. Wu, L. Wang, H. Zheng, J. F. Mitchell, and C. Leighton, Phys. Rev. B **74**, 134408 (2006).
- [47] For a review see T.R. McGuire and R. J. Potter, IEEE Trans. Magn. **MAG-11**, 1018 (1975) and references therein.
- [48] G. Peral, J. Colino, J. M. Alameda and J. L. Vicent, J. Appl. Phys. **73**, 6390 (1993); J. Moritz, B. Rodmacq, S. Auffret and B. Dieny, J. Phys. D: Appl. Phys. **41**, 135001 (2008).
- [49] F. Valdés-Bango, F. J. García-Alonso, G. Rodriguez-Rodriguez, L. Moran-Fernandez, A. Anillo, L. Ruiz-Valdepeñas, E. Navarro, J. L. Vicent, M. Velez, J. I. Martin and J. M. Alameda, J. Appl. Phys. **112**, 083914 (2012).
- [50] E. A. Jagla, Phys. Rev. B **72**, 094406 (2005).
- [51] J. E. Davies, O. Hellwig, E. E. Fullerton, G. Denbeaux, J. B. Kortright and K. Liu, Phys. Rev. B **70**, 224434 (2004).
- [52] A. Hierro-Rodriguez G. Rodriguez-Rodriguez, J. M. Teixeira, G. N. Kakazei, J. B. Sousa, M. Velez, J.I. Martin, L. M. Alvarez-Prado and J. M. Alameda, J. Phys. D. Appl. Phys. (submitted).
- [53] L. M. Alvarez-Prado and J. M. Alameda, Physica B **343**, 241 (2004).
- [54] F. Chiodi, J. D. S. Witt, R. G. J. Smits, L. Qu, G. B. Halász, C.-T. Wu, O. T. Valls, K. Halterman, J. W. A. Robinson and M. G. Blamire, Europhys. Lett. **101**, 37002 (2013).
- [55] F. E. Harper and M. Tinkham, Phys. Rev. **172**, 441 (1968).
- [56] J. L. Vicent, S. J. Hillenius, and R. V. Coleman, Phys. Rev. Lett. **44**, 892 (1980).
- [57] H. J. Herrmann, B. Derrida and J. Vannimenus, Phys. Rev. B **30**, 4080 (1984).
- [58] D. He, N. N. Ekere and L. Cai, Phys. Rev. E **65**, 061304 (2002).
- [59] A. Coniglio and H. E. Stanley, Phys. Rev. Lett. **52**, 1068 (1984).